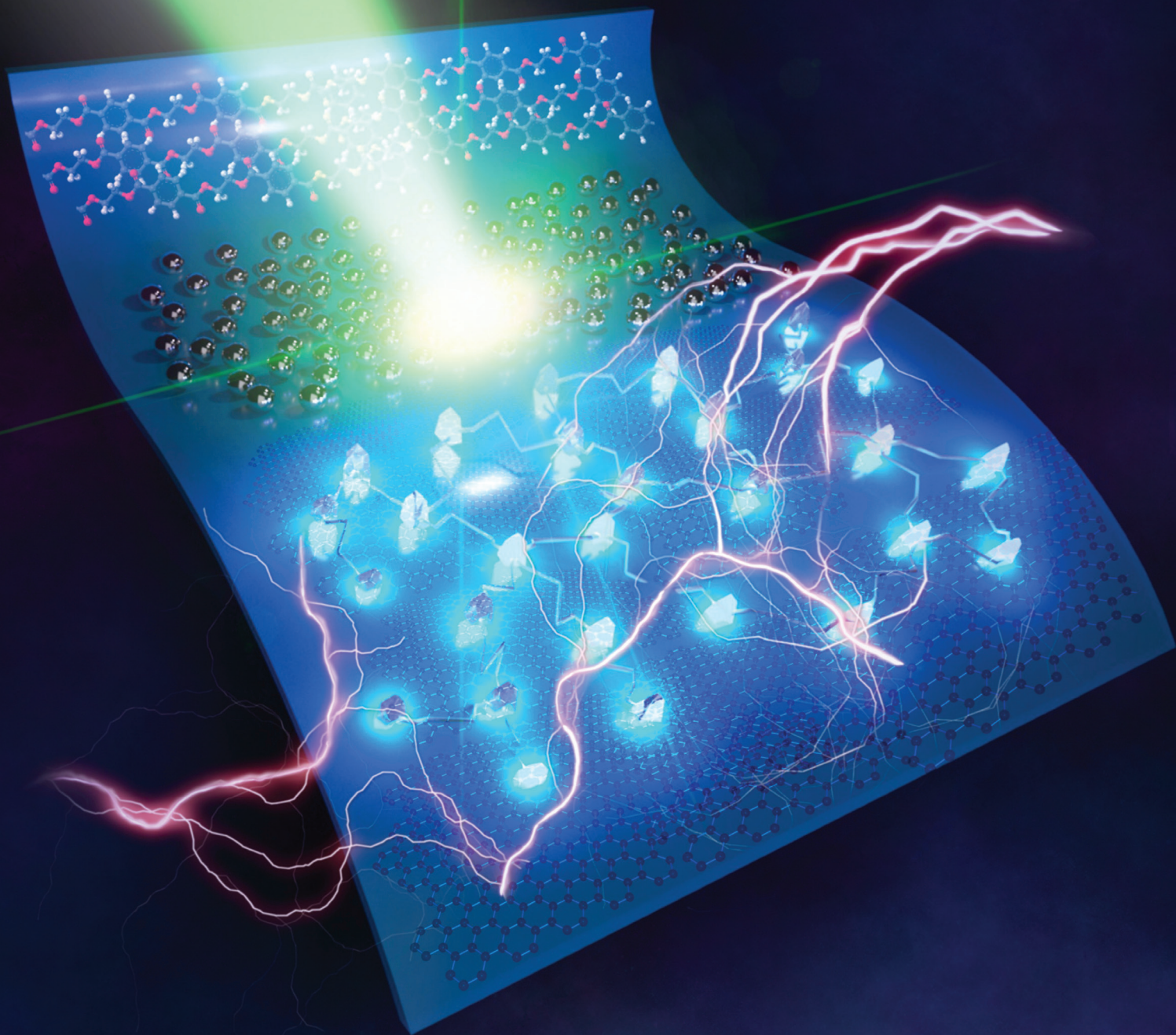


ADVANCED FUNCTIONAL MATERIALS



Ultra-Robust Flexible Electronics by Laser-Driven Polymer-Nanomaterials Integration

Raul D. Rodriguez,* Sergey Shchadenko, Gennadiy Murastov, Anna Lipovka, Maxim Fatkullin, Ilia Petrov, Tuan-Hoang Tran, Alimzhan Khalelov, Muhammad Saqib, Nelson E. Villa, Vladimir Bogoslovskiy, Yan Wang, Chang-Gang Hu, Alexey Zinovyev, Wenbo Sheng, Jin-Ju Chen, Ihsan Amin, and Evgeniya Sheremet

Polyethylene terephthalate (PET) is the most widely used polymer in the world. For the first time, the laser-driven integration of aluminum nanoparticles (Al NPs) into PET to realize a laser-induced graphene/Al NPs/polymer composite, which demonstrates excellent toughness and high electrical conductivity with the formation of aluminum carbide into the polymer is shown. The conductive structures show an impressive mechanical resistance against >10000 bending cycles, projectile impact, hammering, abrasion, and structural and chemical stability when in contact with different solvents (ethanol, water, and aqueous electrolytes). Devices including thermal heaters, carbon electrodes for energy storage, electrochemical and bending sensors show this technology's practical application for ultra-robust polymer electronics. This laser-based technology can be extended to integrating other nanomaterials and create hybrid graphene-based structures with excellent properties in a wide range of flexible electronics' applications.

expected to impact society profoundly. These life-changing technologies require the development of new materials that exhibit superior mechanical, chemical, and electrical stability while being non-toxic and inexpensive to produce on a large scale. In this context, polymers have become a curse and a blessing, a curse because of their widespread use and the waste issues that come with that, polluting different environments not only urban but also critical ecosystems from oceans to deserts. The blessing comes from the inexpensive implementation of various goods, from medical devices and clothing to electronics. Inexpensive manufacturing enabled by polymer processing technology had profound socio-economic implications by making consumer products affordable to low-income sectors. To

1. Introduction

Nowadays, we live in one of the most exciting times where the revolution in technology, such as the Internet of Things, wearable electronics, and neural-computer interfaces, is


introduce additional functionality, nanomaterials such as metal nanoparticles, quantum dots, or carbon nanotubes and graphene are integrated into polymers by the thermal or chemical processing of polymer pellets monomers with the polymerized material acting as a matrix for the nanomaterial phase.^[1–3] We also have demonstrated surface polymerization on graphene and other 2D layers with diverse technological applications.^[4–6] However, implementing these and other conventional methods is neither environmentally friendly nor cost-effective. Moreover, conventional electronic devices require spatial structuring with traditional fabrication methods, including photon and electron lithography. These methods are expensive, difficult to operate, and require the use of preformed masks. On the other hand, laser-driven approaches for the fabrication of flexible electronics are gaining momentum in recent years,^[7] mainly because of the scalability and the advantage of the mask-less formation of arbitrary patterns^[8] while providing better spatial resolution than liquid processing approaches such as inkjet printing.^[9,10] These laser-based approaches include the synthesis of conductive silver patterns on polyimide^[11] and polyurethane,^[12] crystallization of BiVO₄ films,^[13] carbonization of organic particle films on PET,^[14] and metallization of a Cu-containing polymer,^[15] and photothermal annealing of indium zinc oxide on different polymers.^[16] The introduction of different materials in the bulk polymer was exploited to enable laser processing for polymer

Prof. R. D. Rodriguez, S. Shchadenko, G. Murastov, A. Lipovka, M. Fatkullin, I. Petrov, T.-H. Tran, A. Khalelov, M. Saqib, N. E. Villa, V. Bogoslovskiy, A. Zinovyev, Prof. E. Sheremet
Tomsk Polytechnic University
30 Lenin Ave, Tomsk 634050, Russia
E-mail: raul@tpu.ru

Y. Wang, C.-G. Hu, Prof. J.-J. Chen
School of Materials and Engineering
University of Electronic Science and Technology of China
Chengdu 610054, China

Dr. W. Sheng
Leibniz Institute of Polymer Research Dresden e.V.
Dresden 01069, Germany

Dr. I. Amin
Van't Hoff Institute of Molecular Science
University of Amsterdam
Science Park 904, Amsterdam 1098XH, The Netherlands

 The ORCID identification number(s) for the author(s) of this article can be found under <https://doi.org/10.1002/adfm.202008818>.

DOI: 10.1002/adfm.202008818

marking, including additives such as graphene/polystyrene,^[17] antimony trioxide polystyrene,^[18] TiO₂ nanoparticles,^[19] and oxides like Fe₃O₄, ZrO₂,^[20] and SnO₂.^[21] For this application, the laser-driven embedding of dyes into the surfaces of polymers is particularly interesting by combining spray coating with laser curing for marking purposes.^[22] Soppera's group innovative approach contrasts previous works that included the dye or light-absorbing nanoparticle system in the whole bulk of the polymer matrix. However, in all these examples for the laser marking of polymers, the additives were only used to increase the photon absorption inside the composite. Going beyond that application, we envisage that laser processing of polymers that are typically transparent to laser irradiation could induce the formation of electrically conductive nanostructures. This processing gives rise to the so-called laser-induced graphene (LIG) but with the critical aid of a nanoparticle film acting as a photothermal transducer. To address this question, here we prepared Al nanoparticle films deposited on PET with a systematic investigation of the chemical, microstructure, and structural properties that occurred after laser processing. We hypothesize that an Al NP film can have the same photosensitizing effect as other additives shown before in the works discussed above. Al NPs showed localized surface plasmons resonance (LSPR) in the UV-blue range^[23] that could match the light excitation energy used in laser processing. Moreover, we anticipate that the photothermal energy induces the formation of carbon conductive structures and their physical integration into the polymer surface in a single-step, giving rise to a conductive network. We also analyzed the mechanical performance of the laser-induced structures we obtained and demonstrated their applications in flexible electronics. These findings let us propose that the mechanical properties of such an electrically conductive and integrated graphene/nanoparticle/polymer composite would be superior to any other polymer/surface processing available until now. The concept presented here will make sustainable developments in robust, lightweight, flexible, and wearable electronics possible.

2. Results

To make the proof-of-concept laser-driven integration of nanomaterials into PET, we focused on aluminum nanoparticles (Al NPs) since they are inexpensive and readily available as the second most-produced metal in the world.^[24] Because of oxidation in the air, an aluminum oxide layer is formed at the outermost surface, making films made from these nanoparticles poorly conductive. We verified the untreated Al films' low conductivity to be above the MOhm range due to its oxide layer's insulating effect. After laser irradiation, we found a significant increase in the laser-induced metal-polymer composite (LIMPC) conductivity and remarkable mechanical stability. We determined that the conductivity and surface roughness could be controlled by adjusting the average laser power (see Note 1, Figures S1 and S2, Supporting Information). Also, we propose that Al NPs act as photothermal transducers during the laser treatment, converting laser energy into localized heating, leading to the graphitization of PET, and also serving as plasmonic light and heat sources when illuminated by a laser. To sum up,

we propose several simultaneous processes triggered by laser irradiation that could lead to the fabrication of a highly robust and conductive graphene/Al/PET composite. This mechanism includes local melting of PET, integration of Al NPs into the top PET layer, Al oxidation and bonding of Al NPs with PET oxygen functional groups, LIG formation at the interface of PET/Al NPs using the polymer matrix as carbon precursor, and Al₄C₃ formation because of high local temperature and pressure. We investigate this mechanism with a battery of chemical, mechanical, and physical analyses discussed below. Afterward, we test the performance of LIMPC in several flexible electronics' applications.

2.1. Chemical and Structural Characterization Tells the Mechanism of LIMPC Formation

We combined different structural, spectroscopic, and chemical analyses to establish a fundamental description of the formation mechanism of this new hybrid material. Raman spectroscopy is a critical tool for investigating carbon nanomaterials, particularly for confirming graphene's presence in a sample. The Raman spectrum in **Figure 1a** obtained from an LIMPC sample provides the first evidence for laser-induced graphitization and graphene formation. Graphene D, G, and 2D fingerprint peaks^[25] are clearly visible at 1347, 1589, and 2689 cm⁻¹ in the Raman spectrum. These results validate our hypothesis showing that we obtain graphitic carbon beyond an amorphous phase that could be expected from the photoinduced high-temperature decomposition of PET. This also shows the power of Raman in the study of graphene-based materials since if we would have only amorphous carbon, then we should see broad D and G bands, an amorphous signature below 800 cm⁻¹, and a much weaker 2D peak.^[26] The D/G intensity ratio (I_D/I_G) allows us to evaluate the defect density per square centimeter using $n_d^2 = \frac{5.9 \cdot 10^{14} [\text{cm}^{-2} \text{eV}^4]}{E_L^4 [\text{eV}^4]} \left(\frac{I_D}{I_G} \right)^{-1}$ where E_L is the laser energy ($\lambda = 532 \text{ nm} \rightarrow E_L = 2.33 \text{ eV}$).^[25]

This gives us an estimation for the defect concentration in our laser-induced carbon lattice in LIMPC of ca. $5.6 \cdot 10^5 \text{ cm}^{-2}$. The defect concentration (and thus the graphene quality) for LIMPC matches the value observed for LIG made by CO₂ laser irradiation of polyimide (PI).^[27] Defect evaluation is important since a compromise between defect concentration and electrical conductivity is essential for applications in sensing and photocatalysis, as we recently found for the case of functionalized graphene-based devices.^[7] We know that without metal catalysts, laser treatment of a polyimide film can induce the formation of graphene-like multi porous structures due to high temperature and pressure achieved during irradiation.^[28] Molecular dynamic calculations show the evolution of carbon rings in polyimide from 6 member rings to 5 and 7 carbon atoms' radicals when the system reaches $\approx 2100 \text{ K}$. For a higher temperature and longtime process 5 and 7 carbon rings get converted to a 6 member ring with a honeycomb structure, by breaking bonds with O and H atoms that end up released as gases.^[29] In our case with LIMPC, and following the polyimide case, the remaining oxygen and hydrogen atoms that were not released as gas molecules H₂ and H₂O are located at the edges of the

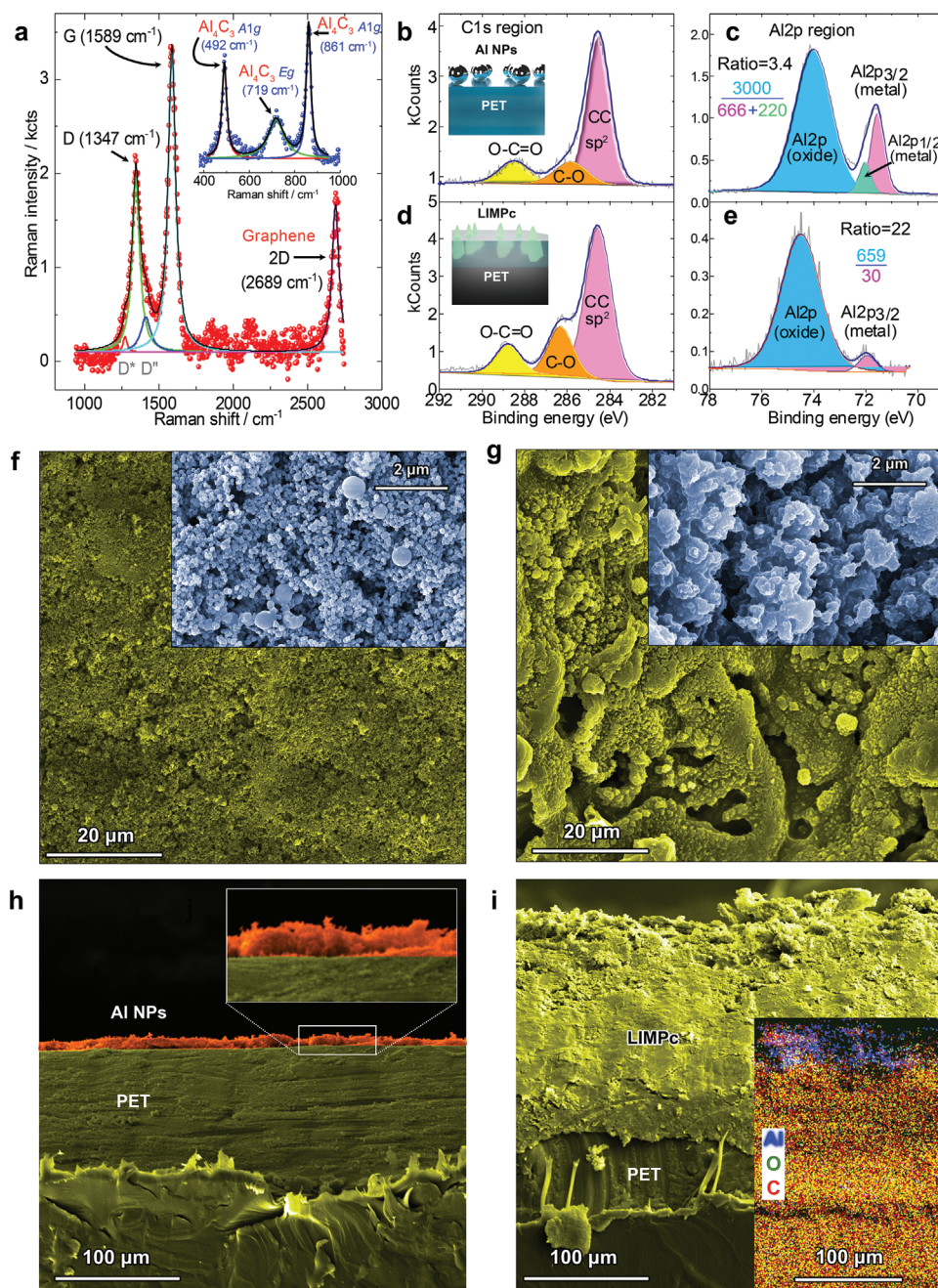


Figure 1. Characterization results of samples with and without laser-induced integration. a) Raman spectrum of the LIMPC sample and the fitting with the main D, G, and 2D peaks of graphene. In the inset is the low-frequency spectrum which matches the A1g and Eg Raman modes of Al₄C₃. The peaks marked with arrows show the two carbon-based materials identified in LIMPC, graphene, and Al₄C₃. X-ray photoelectron spectra around the C1s and Al2p regions for Al nanoparticles on PET, pristine and after laser processing, (b,c) and (d,e), respectively. In the insets are shown the schematic of the Al nanoparticles on b) PET and d) after laser-driven integration. Top imaging of the samples by SEM f) without and g) with laser irradiation, and their respective cross-section images (h) and (i). The color-coded EDX image of the cross-section is shown as an inset in (i).

newly-formed graphene domains. We expect those oxygen atoms to be shared with the PET fragments that were not decomposed. This configuration explains the high mechanical resilience of LIMPC since the graphene network with tunable wetting properties is formed as an intrinsic part of the polymer (Figure S3, Supporting Information). Moreover, the combination of Al particles and graphene sparked significant interest

in the materials science community because of the superior mechanical properties of Al-graphene composites.^[30] The fast rise in temperature and spatial heat confinement around nanoparticles are the ingredients necessary to expect high pressure. The roughness of the structure visible in Figure 1g is evidence of gas release related to high pressure. Thus, the intense conditions of localized temperature and pressure achieved in our

LIMPC obtained by laser irradiation (as also reported for conventional LIG^[28]) promote not only graphene formation and polymer integration of Al NPs, but also the formation of an Al₄C₃ phase. Typically, aluminum carbide can be produced in an electric arc furnace, with -168 kJ mol^{-1} free energy formation at 750°C .^[31,32] It is reasonable to reach this temperature at least locally around the Al NPs photothermal transducers in the case of LIMPC.^[29]

The Al₄C₃ formation was also confirmed recently in the laser sintering of Al particles with carbon nanotubes.^[33] Indeed, the low-frequency Raman spectrum of LIMPC, in the inset of Figure 1a, shows the characteristic peaks from Al₄C₃, confirming the formation of this carbide phase.^[34,35] This is an exciting result since aluminum carbide is an attractive reinforcement material for forming metal matrix composites, which are in high demand by modern aerospace, marine, and automobile industries. The Al₄C₃ phase is lightweight, has a low thermal expansion, high thermal conductivity, stiffness, and strength.^[32] Al₄C₃ is also an abrasive material with high hardness and high thermostability (up to 1400°C), which can be used in high-speed cutting tools. Besides, Al₄C₃ formation provides an interfacial anchoring layer in Al/C (graphite, CNT, graphene derivatives) composites, which improves composite's mechanical properties such as enhancement of specific strength, fracture elongation,^[36] Vickers hardness,^[37] as well as the decrease of thermal expansion coefficient.^[38] This material was never before reported as a product of laser processing in a graphene-polymer composite until now. XPS chemical analysis shows that the sp² carbon level increases slightly after laser irradiation as deduced from the high-resolution scan over the C1s region (Figure 1b–d, respectively). However, that change in Csp² content is not significant enough to explain the system's electrical conductivity since there is a simultaneous rise of sp³ components. Indeed, before irradiation, the Al2p region in XPS (Figure 1c) showed a significant amount of oxide and metallic Al peaks (Figure 1c). Scanning electron microscopy (SEM) images in Figures 1f and 1g show the changes in film microstructure before and after laser processing, respectively. These results clearly show a metallic component. After laser irradiation, both Al oxide and metallic components decrease with an increase in film roughness and porosity after laser processing, which is beneficial for energy storage, catalysis, and sensing. The increase in roughness is partly due to gas release (CO₂, H₂, and water) during laser processing. The most remarkable observation from SEM is the visibility of the spatial extension of the laser-induced changes in the PET surface, as depicted in the cross-section images in Figures 1h and 1i. This is significant because pristine PET is not affected by the laser beam, but a thin NP film, even as thin as $1 \mu\text{m}$, has consequences in the film chemistry, conductivity, and structure that extend into PET. We verified our hypothesis for a plasmonic contribution from Al NPs during laser-processing by optical absorption spectroscopy (UV–vis). We carried out UV–vis experiments for an Al NP dispersion used for film deposition on PET, and for the Al NP film on PET before laser irradiation. UV–vis results for the Al NPs dispersion in ethanol show absorption peaks that match the LSPR observed in other Al nanostructures (see Figure S4a, Supporting Information).^[23] The optical absorption for the Al film on PET in Figure S4b, Supporting Information, shows the light

absorption saturation in the whole UV–vis–NIR range. This wide-range absorption suggests that Al NPs could also work for other laser excitation wavelengths. Although the XPS observations could point to removing the Al particles due to laser ablation, the EDX results in SEM in the inset of Figure 1i (along with XRD, Figure S5, Supporting Information) shows that Al partially remains in the film after laser processing. Thus, the decrease in the Al signal observed in XPS can be assigned to integrating Al NPs into the carbon-rich polymer. The increase in Al particles' oxidation observed after laser processing agrees with the thermal annealing of Al in ambient conditions.^[39] While XPS results show that the metallic Al decreases, and the increase in sp² carbon was not significant, these observations support our hypothesis for forming an interconnected carbon network (that is electrically conductive) where aluminum oxide particles act as connecting nodes.

We further argue that the mechanism responsible for the high electrical conductivity and high mechanical robustness displayed by our laser-processed structures is the same. We support this conclusion by considering that aluminum oxide or aluminum carbide cannot be responsible for the high electrical conductivity. While Al₂O₃ is a dielectric, Al₄C₃ is a semiconductor with a bandgap ranging from 1.3 to 2.4 eV.^[35,40] EDX results (see inset in Figure 1i and Figure S6, Supporting Information) show that Al is present throughout the 20–30 μm of the laser-induced composite (the LIMPC thickness depends on the initial metal film thickness and laser irradiation parameters). In contrast, XPS shows that after laser irradiation Al is mostly in its oxidized form with a sixfold increase of the oxide component (2p peak area) with respect to metallic Al (2p_{3/2} and 2p_{1/2} peaks), see Figure 1c–e and Figures S7 and S8, Supporting Information. The presence of a large outer oxide shell is directly evidenced by TEM results with elemental mapping shown in Figure S9, Supporting Information. In addition, Raman and XRD show the formation of a carbide phase. Thus, the conductivity must arise from another component in the film. These observations make us reconsider the role played by the slight increase in sp² carbon content. Besides Al's presence, the EDX results also show carbon in the whole LIMPC structure, supporting our hypothesis for the formation of a 3D electrically conductive network. XPS results in the C1s region show that laser processing increases the C–O sp³ content from exposing PET, acting as a matrix for the Al-carbon network generated. This integration gives rise to high electrical conductivity (due to sp² carbon) and high mechanical resilience (due to anchoring with Al₄C₃), resulting in a conductive polymer composite firmly incorporated to PET as shown schematically in **Figure 2**. To further evidence the nature of LIMPC, we designed an experiment in which PET was chemically dissolved to expose the remaining LIMPC. This freestanding LIMPC sample was investigated by SEM, EDX (Figure S10, Supporting Information), and transmission electron microscopy (TEM), see results in Figure S9, Supporting Information. Our microscopy results with elemental compositional mapping provide direct evidence for the 3D graphene network formed around Al-based composites. We verified the electrical conductivity of this PET-free sample confirming the conductive nature of this 3D network. Besides the low sheet resistance of 181 Ohm sq^{-1} measured using the transmission line measurement technique (Figure S11, Supporting

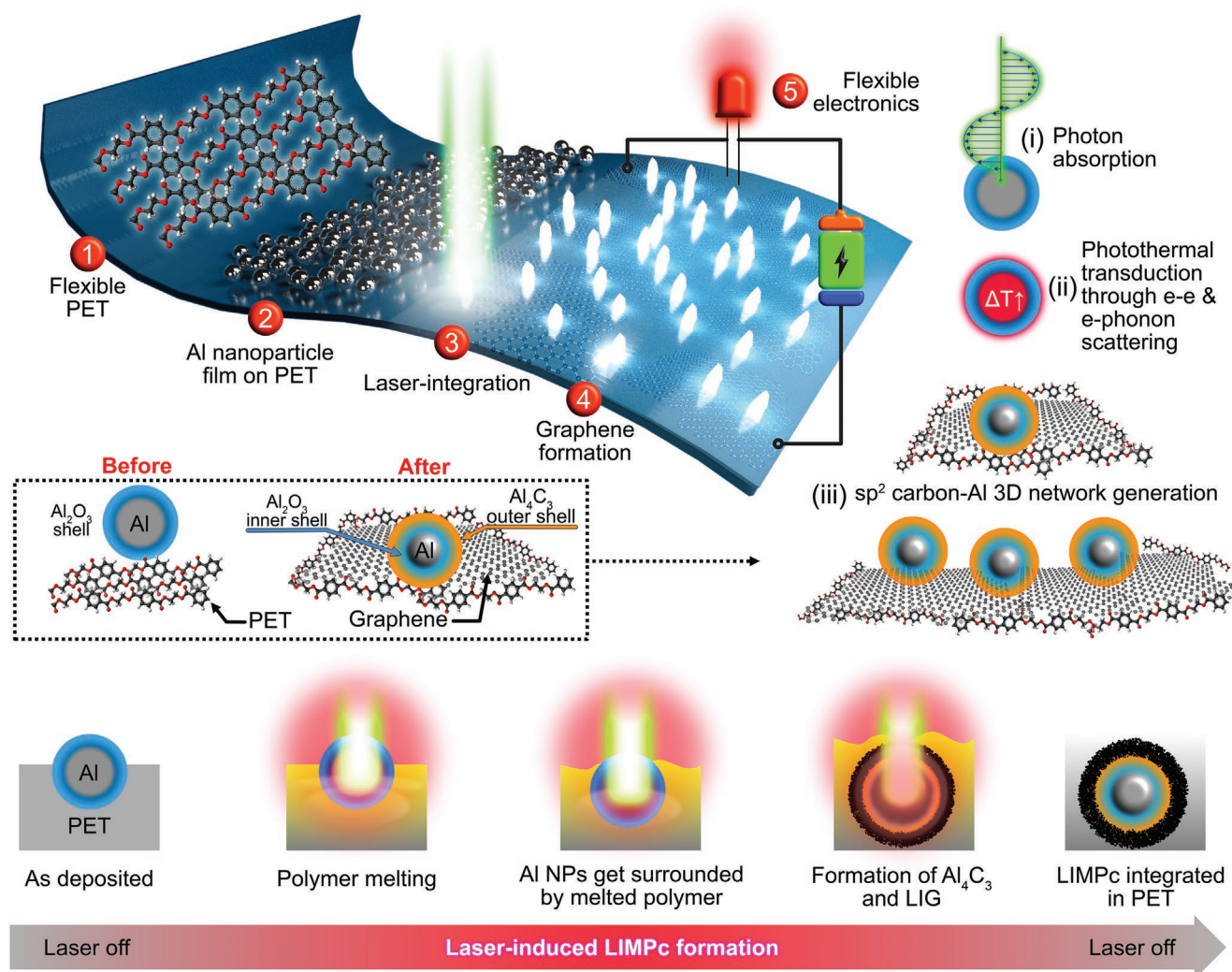


Figure 2. Illustration of the laser-induced integration of nanomaterials into PET. 1) A flexible substrate is 2) coated by a thin film of Al nanoparticles that act as photothermal transducers 3) for their integration into the polymer substrate and 4) graphene generation. 5) The laser-induced composite is electrically conductive allowing robust applications in flexible electronics. The mechanism of formation involves i) photon absorption by the Al NPs, ii) relaxation of photoexcited-charge carriers through electron–electron and electron–phonon scattering that results in a localized temperature increase. iii) The high temperature induces the thickening of the Al_2O_3 shell, appearance of an Al_4C_3 interface, graphene formation, and anchoring to the remaining PET through oxygen groups at the edge of the newly-formed graphene. At the bottom, we show schematically the different processes proposed to occur during laser irradiation.

Information), we tested the high mechanical robustness of LIMPC in the next section.

2.2. Mechanical Resilience

To explore the limits of LIMPC and confirm the extraordinary integration, we performed a set of experiments to evaluate this material's mechanical resilience in **Figure 3a–d**. We recorded the electrical resistance and optical microscopy images from the samples before and after the abrasion test, see **Figures 3b** and **3c**, respectively. As a reference, we also analyzed the behavior of a PET substrate with a conductive silver film, which is the standard conductive material used in flexible electronics (shown as insets in the optical microscopy

images in **Figure 3**).^[41] We evaluated the changes in resistance as $\Delta R [\%] = \frac{R_f - R_0}{R_0} \cdot 100\%$, where R_f and R_0 are the film's resistance values after and before the abrasion test, respectively. The silver electrode's initial resistance value on PET was $3.5 \, \Omega$ and after the test, the resistance increased beyond the range of our resistance meter of $2 \, \text{M}\Omega$. Surprisingly, the LIMPC electrode did survive the harsh abrasion for 72 h, although the resistance increased almost twofold (see **Figure S12**, Supporting Information). We explain this increase in resistance as due to the abrasion of the topmost conductive composite layer and nanoparticles protruding from the LIMPC surface (as shown in the SEM results, **Figure 1i**). The LIMPC electrode passing this test so well can be attributed to a robust interpenetrated Al– Al_2O_3 – Al_4C_3 –graphene network firmly integrated into PET as

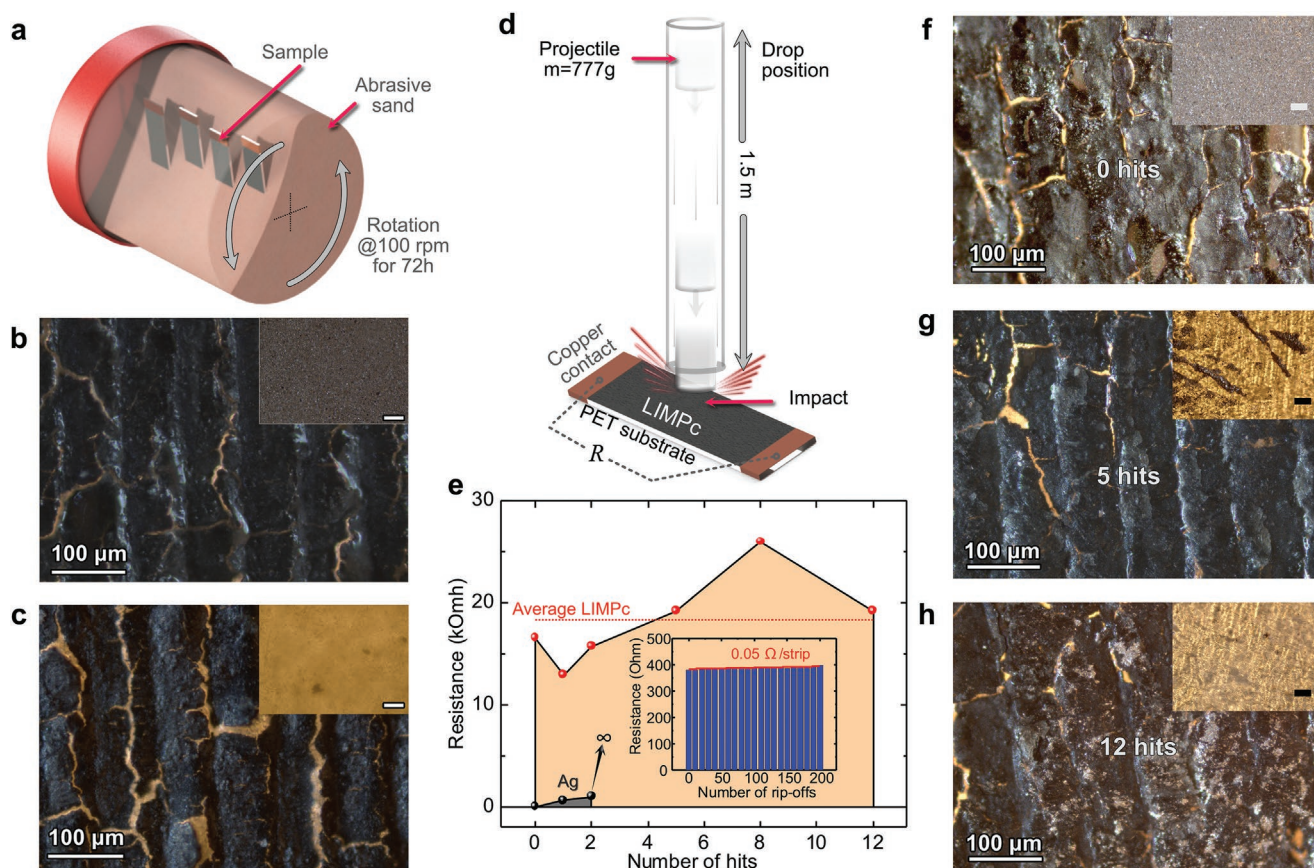


Figure 3. Mechanical performance evaluation of LIMPc. a) Sketch of the sample for the abrasion test (abrasive, 0.5 mm grains of dry sand, rotated continuously at 100 rpm for 72 h). Optical microscopy images of LIMPc obtained b) before and c) after the test. d) Schematic illustration of the impact test with a projectile dropped up to 12 times on LIMPc and on an Ag film on PET (samples size is 30 mm × 8 mm²). e) Resistance changes after several impact events for LIMPc (red circles) and Ag/PET (black circles). For silver, after three impacts the film is not conductive anymore. In the inset is shown the resistance values for LIMPc after up to 200 stripping events (rip-offs with adhesive tape). Optical microscopy images after a different number of projectile impacts: f) 0 hits, g) 5 hits, and h) 12 hits. In the insets are shown the images for Ag films on PET subject to the same conditions with the scale bars of the same magnitude as in the main images.

schematically illustrated in Figure 2. Furthermore, we employed this abrasion test to study the performance of reduced graphene oxide films and silver paste on PET. However, these films did not withstand the test compared to LIMPc as could be seen in Figures S13 and S14, Supporting Information. Besides the abrasion test, we performed further mechanical examination by subjecting the LIMPc electrodes to projectile impact tests as depicted in Figure 3d (see also Figures S15 and S16, Supporting Information).

Electrical resistance was measured before and after each impact test; the results are shown in Figure 3e. Figure 3f shows the optical microscopy images of the sample before the impact test (0 hits), and after 5 and 12 hits, Figures 3g and 3h, respectively. The inset images correspond to an Ag film on PET of the same dimensions as LIMPc and subjected to the same test conditions. In contrast to LIMPc, the silver film did not survive the test after three impacts and became nonconductive (see black circles in Figure 3e). The optical microscopy images in Figure 3 evidence the presence of cracks in LIMPc. We explain these cracks as due to the thermal mismatch between the bulk PET substrate and the Al nanoparticle (NP) film, similarly to graphene formation in LIG from Kapton.^[42] During laser

processing, photothermal heating^[43] results in the melting of the topmost volume of PET substrate (260 °C), which induces partial engulfing of the Al NP film by melted PET. The LIG, which starts at the interface between PET and the Al NP film, will cool down after the laser irradiation step is finished. Similarly, the melted PET at the surface that was not transformed to LIG resolidifies. It is during this cool-down process that because of the thermal expansion coefficient mismatch between the PET (2×10^{-5} – 8×10^{-5} K⁻¹) and LIG (8×10^{-6} K⁻¹) built-in strain will be relaxed by the deformation of the interface resulting in the cracks we observed. The cracks could be controlled by optimizing the laser processing parameters, although not completely avoided due to the thermal expansion mismatch discussed above. We figured that these cracks could be beneficial to our material applications' such as in energy storage and sensing due to the enhanced surface exposure in a film with cracks than in a crackless smooth film. Thus, in this work, we did not aim at controlling cracks since they did not affect the electrical conductivity much. Instead, we focused on optimizing the laser processing conditions to achieve the highest degree of integration and electrical conductivity.

To complement the abrasion and impact tests, we also performed three more simple procedures to verify the mechanical

robustness of LIMPC. First, we sonicated the LIMPC sample in distilled water for an extended period of up to 15 min. After sonication, we did not notice visible changes in surface morphology, and the resistance values were the same as before. Second, we made a mechanical stripping test using strong adhesive tape. The experiment showed that after 200 consecutive stripping events, we observed no significant changes in surface morphology or electrical conductivity (see the inset of Figure 3e and Note 4, Supporting Information). Finally, we used a thinner PET (0.1 mm instead of 0.65 mm) to evaluate how the substrate thickness affects the LIMPC mechanical robustness. The SEM cross-section in Figure 1i shows that the PET substrate could get modified up to 100 μm deep. Thus, for 0.1 mm thick PET or thinner, the whole substrate should be transformed to LIMPC. This is exactly what we observed in our experiments, and in this case, LIMPC was not as mechanically robust as when using a thicker PET film, which shows that the PET substrate thickness is another parameter to control the mechanical properties of LIMPC. These results evidence the potential of our material's use in various conditions limited only by the strength and thickness of PET used here as a substrate and carbon source.

2.3. Applications in Flexible Electronics

Owing to the impressive mechanical robustness of our LIMPC material, we designed and constructed several device prototypes for applications in flexible circuits, flexors, electrothermal heating elements, electrochemical sensors, and photocatalysis. These results are summarized in Figure 4. We started by demonstrating laser-patterned flexible electrical circuits on PET. Figure 4a shows transparent polymer substrate patterning with a high contrast TPU logo and a simple rectangle. The drastic change of PET optical properties after laser irradiation in the presence of metal NPs and graphene in the polymer matrix was widely studied for marking purposes. However, in our case, we also show the high electrical conductivity of arbitrary-shaped circuits. The flexible and conductive patterns are capable of wiring different devices like the LEDs and micro-LEDs shown in Figure 4a. In combination with excellent mechanical robustness, high conductivity makes a perfect foundation for applying such types of sensing devices as flexors. In this regard, we tested our flexible conductive circuit under hundreds of bending cycles and confirmed that there was no degradation of electrical properties. Figure 4b presents the resistance values obtained while bending the device (10 consecutive times) at different radii shown in the x -axis as their reciprocal (see also Figure S17, Supporting Information). The resistance increased by decreasing the bending radius. We found an inversely proportional dependence between these two magnitudes with a proportionality coefficient of 6.3 $\text{k}\Omega \text{ mm}^{-1}$ deduced from a linear fit. Figure S18, Supporting Information, shows SEM images of samples before and after 4000 bending cycles evidencing the mechanical stability of the surface microstructure. As a next step and further demonstration, we fabricated flexors by the laser integration of Al NPs to a more flexible polymer—3D-printed polyethylene terephthalate-glycol (PETG) (see Figure S19, Supporting Information). Combining two promising approaches, such as 3D printing and laser patterning,

provides more freedom in terms of design and functionality of the devices. Here we demonstrated an LIMPC/PETG for robot control using finger gestures (see Figure S20 and video demonstration, Supporting Information). By flexing and extending the finger with a sensor based on LIMPC the resistance values change and activate the robot's motion. This result shows a promising area of applications in robotics and actuators that are now under development in our lab.

The mechanism for the strong interface bonding that allows these applications is rather straightforward. Photothermal heating during laser processing induces the partial melting of the topmost PET in contact with the Al NP film. Thus, under laser irradiation, the Al NP film gets surrounded by melted PET. While a part of this melted PET is used as the carbon precursor for LIG formation, the PET chains further away from the hottest regions do not transform to LIG. When cooling, the newly-formed LIMPC becomes fused with the substrate after the remaining melted PET solidifies. Besides this laser-induced integration, there is a chemical component that enhances mechanical properties. Kawahito et al. showed that not only the anchor (mechanical bonding) effect but also van der Waals interaction and chemical bonding occurred at the boundary between Si_3N_4 ceramic and PET during laser irradiation.^[44] They also showed similar results for titanium and PET.^[45] These collective processes, depicted at the bottom of Figure 2, are the origin of the Al NP integration into the polymer and the strong interfacial bonding that occurs with LIG formation. This mechanism involving different processes is deduced by putting together the spectroscopic results and the direct visualization of the nanoscale composition and spatial distribution in LIMPC discussed above in Section 2.1.

Inspired by the work of Bobinger et al.,^[46] we constructed a flexible electrothermal element based on LIMPC. For this, we used a Kapton substrate that can tolerate higher temperatures than PET, which is also conventionally used for LIG production. Figure 4c (and Figure S21, Supporting Information) demonstrates a superior electrothermal transduction efficiency of LIMPC/LIG with respect to LIG alone. An LIMPC thermal heater reaches a temperature above 112 $^{\circ}\text{C}$ while applying a power of 600 mW. At the same time, the maximum value for LIG is only 40 $^{\circ}\text{C}$ for the same power value. This contrast could be partly explained by a significant difference in resistance between those two devices. For the LIMPC/LIG heater, the resistance value is 194 Ω , while for LIG it is 4 $\text{k}\Omega$. The calculated transformation coefficients (electrical energy to heat) are $8.9 \times 10^{-2} \text{ K mW}^{-1}$ for LIMPC/LIG and $0.9 \times 10^{-2} \text{ K mW}^{-1}$ for LIG. The spatial control of the polymer electrical properties utilizing laser irradiation was further used to fabricate an electrochemical sensor (Figure 4d and Figure S22, Supporting Information). Our sensor integrates three electrodes out of the same material and in the form of screen-printed electrodes widely used in flexible architectures for electrochemical sensing.^[47] The CV curve obtained during the sensing measurements demonstrates a typical behavior for potassium ferricyanide detection, indicating two clear redox peaks.^[48] The high sensitivity is justified by the current value exceeding 1 mA. The clear CVs recorded from electrochemical sensors, and especially current values in the mA range (taking into account that measurements were in a liquid drop), inspired us further to use LIMPC

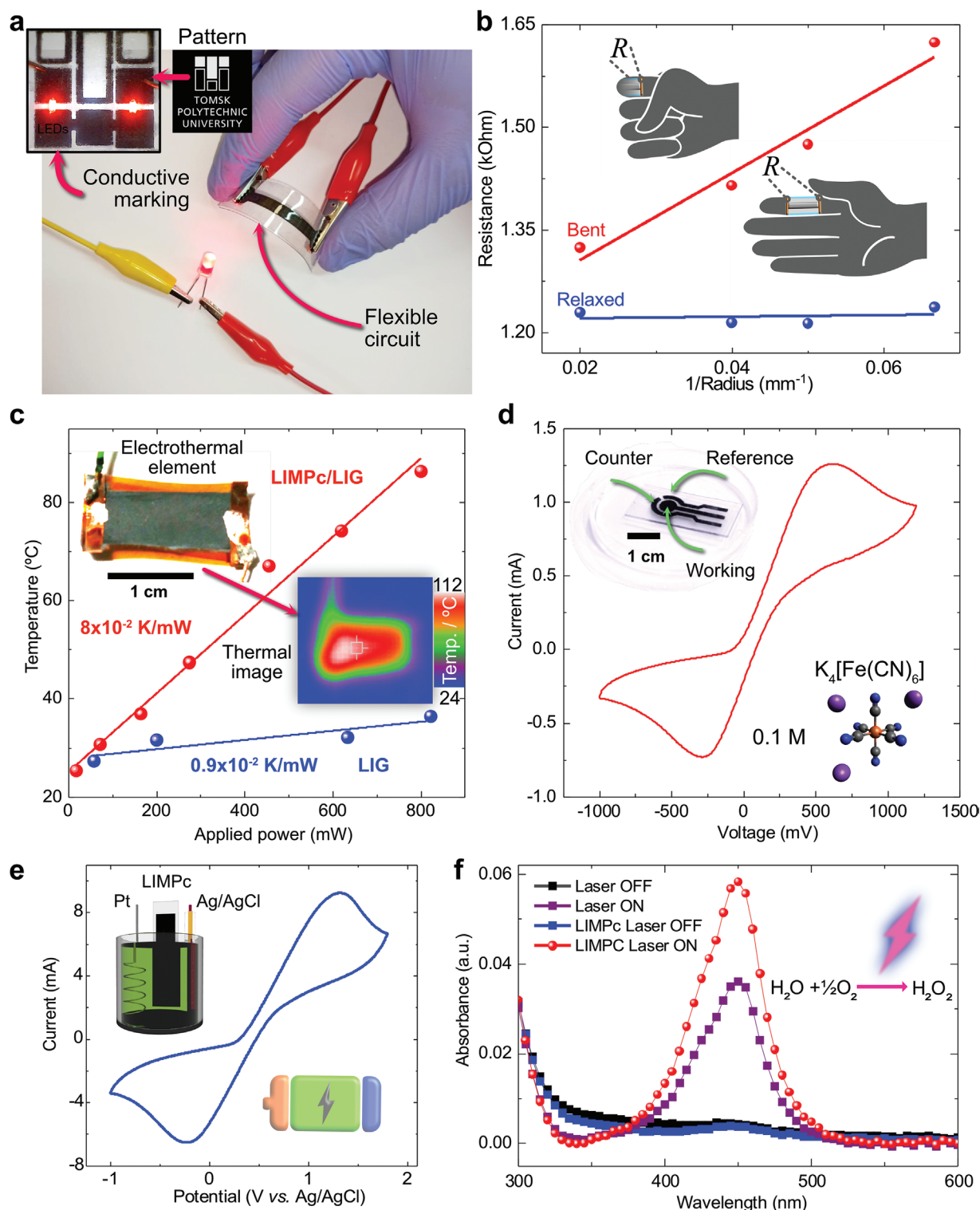
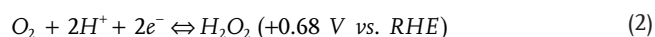
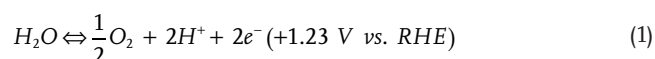


Figure 4. LIMPC applications in flexible electronics. a) A snapshot of a flexible circuit bent and powering an LED; the inset shows a conductive marking made on PET powering two LEDs. b) Electrical resistance at different bending radii for an LIMPC flexible circuit. This device was used to build finger-controlled flexors depicted in the insets and shown in Figure S12, Supporting Information. c) Temperature versus input power for an LIMPC-LIG (red) and LIG (blue) electrothermal heaters made under the same conditions for performance comparison. The figure includes the real image of an electrothermal heater and the thermal image of the sample under external potential. d) A picture of an electrochemical sensor and CV demonstrating the electrochemical detection of 0.1 M ferricyanide. e) Electrochemical characterization of the LIMPC electrode for energy storage applications, including the sketch of the experimental setup. f) Absorption spectra of the TMB-H₂O₂ with and without LIMPC in the dark and under laser irradiation illustrating the application in photocatalysis.

as a material for supercapacitors. We built a 3-electrode cell to demonstrate this application and used our LIMPC as the active electrode (Figure 4e and Figure S23, Supporting Information). To test the electrode performance, we used redox ($K_4[Fe(CN)_6]$) and non-redox (KCl) electrolytes. Both systems allowed us to get symmetric curves with high current values in a potential window of 2 V. The capacitance values reached 41.89 mF cm^{-2} in the case of $K_4[Fe(CN)_6]$, and 4.35 mF cm^{-2} for KCl. These values are superior in comparison to $2.6 \text{ } \mu\text{F cm}^{-2}$ obtained for LIG-based supercapacitor electrodes.^[49] Our results are promising for electrode implementation in robust and flexible supercapacitors.

Finally, we demonstrated the application of LIMPC for photocatalysis. Hydrogen peroxide is an important substance for energy generation,^[50] biological systems,^[51,52] wastewater treatment,^[53] food and pharmaceutical industries,^[54–56] and a biomarker for detecting chronic pulmonary diseases.^[57,58] H_2O_2 also attracts increasing interest as a liquid solar fuel because of its ease of storage, transport, and to generate electricity^[59] in a sustainable and environmentally-friendly way. In principle, hydrogen peroxide can be abundantly-produced from water by photocatalysis. In this work, we used 3,3',5,5'-tetramethylbenzidine (TMB) to detect H_2O_2 by colorimetry.^[60] Figure 4f demonstrates that without laser irradiation TMB is hard to oxidize; thus, the peak of oxidized TMB is insignificant. While under laser irradiation, we clearly observe the characteristic peak at 450 nm, attributed to the oxidized TMB in the acidic medium. The appearance of this peak indicates the presence of hydrogen peroxide.^[60,61] In the presence of LIMPC, the concentration of the oxidized TMB increases almost twice, which means that the amount of hydrogen peroxide also increases twice. The physical origin of this reaction is related to the plasmonic photoexcitation of holes and electrons in aluminum nanoparticles that are resonant under the wavelength used in this work.^[62] We can describe the mechanism of H_2O_2 photocatalysis as follows:



The photoexcited holes diffuse to the sample surface oxidizing water molecules to produce molecular oxygen (Equation (1)). Then, electrons induce the reduction of oxygen to generate H_2O_2 (Equation (2)).^[63] After that, OH radicals generated by H_2O_2 oxidize TMB as confirmed by the appearance of the peak at 450 nm in Figure 4f. The photocatalytic activity of LIMPC is similar to the $ZnIn_2S_4$ monolayer with S vacancies.^[64] In our experiment, we need to consider that although we measured the whole bulk of the solution to deduce the amount of TMB that was oxidized (Figure 4f), during photocatalysis, only a fraction of the bulk solution was in contact with the LIMPC surface where H_2O_2 was generated. Therefore, this result shows that LIMPC has an excellent photocatalytic activity for the generation of H_2O_2 since it doubles the concentration of the oxidized TMB, and this difference comes only from molecules at the LIMPC surface. Laser processing with 3D printing will allow us to develop 3D structures that maximize the surface

area exposed to the molecules we wish to catalyze.^[65] This is an ongoing investigation in our group by combining inexpensive but efficient materials with a novel and large-scale integration strategy.^[66]

3. Conclusions

We prove for the first time the generation of ultra-robust flexible electronics integrating metal nanoparticles, carbide, and graphene formation in one single laser processing step. Besides the focus on Al nanoparticles, the universality of this new concept depicted in Figure 2 was demonstrated with other nanomaterials. We show that the fabrication of different flexible devices is realizable, and withstands thousands of mechanical deformation cycles (Figure S16, Supporting Information), projectile impact, abrasion, scratching, and even chemical attacks by the different solvents used throughout this study. Contrary to the work of Brengersman^[67] who reported a way to preserve the properties of sulfonated membranes using LIG formation, in this work we show a way to add functionality to polymer materials largely used in packaging, textiles, and in consumer electronics. In our case, the laser processing did not result in the sublimation of Al NPs but the integration of Al NPs into the polymer surface. We achieved this integration without the use of thermal annealing or high pressure as recently reported for 3D graphene-Cu networks.^[68] Besides the energy-efficiency benefits, the spatial patterning capabilities are an additional plus that makes our method attractive for electronics implementation and other applications, including temperature sensors (Figure S24, Supporting Information). Beyond the photothermal and mechanical benefits from Al NPs, we further exploit their photonic properties in the photocatalytic oxidation of TMB. We thus contribute to the development of inexpensive architectures that can replace silver and gold conventionally used in plasmonics.^[62] This one-step method is safe and is also environmentally-friendly and does not require the use of harsh or other chemicals for processing. The simplicity of the fabrication and the low-cost requirements in terms of equipment and materials make this technology readily available beyond academic labs, from DIY enthusiasts to entrepreneurs allowing fast prototyping of flexible electronic devices much alike to 3D printing. The new concept developed in this work can be easily extended to different nanomaterials and polymers. This generality was shown by the integration of iron oxide nanoparticles and Si nanowires into PET, as shown in Figures S25, S26, and S27, Supporting Information. We are confident that our work will inspire other researchers who later may improve our method further. By optimizing the source material and the irradiation parameters, it will be possible to significantly reduce the electrical resistance of the LIMPC structure while also optimizing the surface chemistry for targeted applications. The polymer materials include polyimide, which is critical for high-temperature applications such as the electrothermal element shown here, and polylactic acid (PLA), which is the main material used in 3D printing technologies. Besides the applications illustrated here, our method's reliability and simplicity of integration are essential for wearable and lightweight applications for which high robustness and stability against physiological

environments are requirements for futuristic applications such as neural-computer interfaces.^[69,70]

4. Experimental Section

Materials: Aluminum nanoparticles (Al NPs) (50 to 70 nm average diameter; CAS AS 7429-90-5) were purchased from Advanced Powder Technologies, Russia, and used as received. Polydispersed silicon nanowires (40 nm diameter, 1–20 μm lengths, >99% purity) were purchased from Sigma-Aldrich and used without further purification. Iron oxide nanoparticles were synthesized by forced hydrolysis of FeCl_3 as reported previously.^[71]

Thin-Film Deposition: Nanoparticle thin films were deposited by the drop-casting method. An aluminum NPs/ethanol dilution was prepared following the concentration of 30 mg mL^{-1} . A solution of silicon nanowires (Si NWs) was prepared by diluting (20 mg) of polydisperse Si NWs in (1 mL) of deionized water. Then, the dilutions were sonicated (120 W output power and 40 kHz) for 15 min at room temperature. Next, the solutions were deposited on polymer substrates (PET, PETG, Kapton) at a rate of 0.5 $\mu\text{L mm}^{-2}$. The resulting liquid films were dried in ambient conditions.

LIMPC Formation: Laser patterning to achieve a laser-induced metal-polymer composite was performed on Al NPs (or other metal NPs) film deposited on the top of PET using a 450 nm wavelength computer-controlled laser diode that operates at 1.6 kHz frequency. The measured average power was 1 W, which could be further controlled by setting up the P and D parameters in the computer-controlled laser program (see Figure S1, Supporting Information). Also, we evaluated the minimal spot size which in our optical system is equal to $\approx 100 \mu\text{m}$. This value was deduced by visual inspection by optical microscopy of spots made with the laser on a thin GO film. The thin solid film samples in PET were irradiated normal to the surface.

Freestanding PET-Free LIMPC Formation: After LIMPC fabrication, the PET in LIMPC was dissolved by immersing the sample in hexafluoro-2-propanol for 1.5 h.

LIMPC Characterization: The structures of LIMPC samples were characterized using different structural, spectroscopic, and chemical analyzes. For the analysis of the chemical composition of the samples, Raman spectra were acquired using a Renishaw inVia Raman microscope with a green laser source (532 nm). The laser beam was focused on the sample using a 50 \times objective.

X-Ray Photoelectron Spectroscopy (XPS): XPS was performed on a Thermo Scientific K-Alpha system with an Al $K\alpha$ X-ray source, with a spot size of 400 μm^2 and pass energies 50 and 200 eV for narrow regions and survey spectra, respectively. Charge compensation was implemented using electron and argon ion guns.

SEM: SEM images were obtained on an Apreo S, Thermo Fisher Scientific SEM.

EDX: EDX scans were collected on Quanta 200 3D, FEI Company with step size 10 eV.

TEM: TEM was performed on the JEOL JEM-2100F system.

UV-Vis: UV-vis spectra were retrieved by using UV-vis spectrophotometer Agilent Cary 60.

XRD: XRD experimental data were obtained using XRD-6000 diffractometer based on $\text{CuK}\alpha$ radiation with a sliding beam. The operating voltage was 40 kV and current to 30 mA.

Optical Microscopy: Optical Microscopy images were acquired by inverted microscope ZEISS Axio Vert.A1 (Carl Zeiss microscope).

Contact Angle Measurements: An 8 μL of deionized water drop was deposited on the sample surface and measured immediately and 1 min after. ImageJ software with a contact angle plugin was used to evaluate the contact angle values. It was repeated four times to quantify the error and deviation for each sample.

Sheet Resistance Measurements of LIMPC: Sheet Resistance Measurements of LIMPC were performed using the transfer length measurements (TLM) method. A pre-patterned mask with a copper film

was prepared with the distance between contact pads equaling 1.6, 3.6, 5.6, and 7.6 mm (Figure S11, Supporting Information).

Mechanical Tests: Three different tests were performed on LIMPC for the mechanical resilience investigation. During the abrasion test, a sample made on a PET substrate ($30 \times 8 \times 0.65 \text{ mm}^3$) was placed in the rotating (100 RPM) container $\frac{3}{4}$ filled with abrasive sand (0.5 mm in diameter) for 72 h as shown schematically in Figure 3. The copper tape and silver paste (Leitsilber L100) were used as an electrical interface for stable resistance measurement. Impact tests were conducted using a steel cylinder with a diameter of 45.88 mm, a height of 59.7 mm, and a mass of 777 g. The cylinder was dropped from a height of 1.5 m hitting the sample placed on a metal plate with an impact energy of 11.4 J (neglecting friction and air resistance). Electrical resistance was measured before and after each strike test.

The last one was a stripping test with strong adhesive tape. Electrical resistance was measured after each rip off iteration.

Device Testing: Bending sensor: This was investigated with a three-point flexural test. A long-engraved stripe-shaped sample with 80 by 4 mm^2 size was created for this experiment. The distance between the two side points was adjusted to 20 mm. The indenter movement was controlled by a microprocessor and a step motor. The bending diameters were 15, 20, 25, and 50 mm. The resistance measurements were obtained for every 10 bend-relax state cycles per constant diameter.

Thermal Heater: A thermal heater was obtained by applying voltage to 20.10 mm^2 LIMPC structure on a Kapton substrate. A thermal image was recorded using a 60 \times 60 pixel camera HT-02 from Hit (China) operating at a 10 cm distance from the sample when 18.4 to 800 mW power was applied.

Electrochemical Sensor: An electrochemical sensor with screen printed electrodes was performed to detect $\text{K}_4\text{Fe}(\text{CN})_6$ in an aqueous solution with a 0.1 M concentration in the potential window from –1000 to 1200 mV and a scan rate 100 mV s^{-1} .

Temperature Sensor: Hot water was poured into a 30 mm flat-bottom glass flask placed on the PET side. The sensor was engraved on another bottom side of the PET substrate to prevent any water-drop influence on measurements. A digital DS18B20 temperature sensor on-chip with a water protection tube was used to read out the temperature from the flask. The resistance of sample versus water temperature was recorded while cooling down in ambient conditions.

Photocatalytic Application: LIMPC was put on a disk, then 5 mL distilled water was dropped on a disk to cover LIMPC. The sample was transferred to a laser irradiation chamber. After that, 100 μL $\text{TMB} + \text{H}_2\text{O}_2$ (Vector, Russia) was dropped on the sample. Then, the sample was irradiated by a laser with wavelength 450 nm and power 50% (ca. 1.5 W nominal power), depth 10% in 40s (circle with $d = 6 \text{ cm}$). After that, LIMPC was taken out of the disk and 100 μL of stop-reagent (H_2SO_4 , Vector, Russia) was dropped on the disk to stabilize the product of TMB oxidation.

Supporting Information

Supporting Information is available from the Wiley Online Library or from the author.

Acknowledgements

This research is supported by the Tomsk Polytechnic University within the framework of the Tomsk Polytechnic University Competitiveness Enhancement Program (VIU-RSHEP-198/2020) and the Sichuan Science and Technology Program (Grant 2018HH0152). The authors thank Prof. Corinne Chaneac from College de France for the iron oxide nanoparticles. The authors are grateful to Dr. Elena V. Dorozhko for the support for the photocatalysis measurement and Prof. Evgenii V. Plotnikov for optical microscopy experiments. The authors thank Dr. Evgenii Galunin for his support with the electrochemical experiments. The authors thank Prof. Fedor Gubarev for providing the Al nanoparticles used at the start of this research.

Conflict of Interest

The authors declare no conflict of interest.

Data Availability Statement

Research data are not shared.

Keywords

laser processing, laser-induced graphene, ultra-robust flexible electronics, wearables

Received: October 16, 2020

Revised: December 15, 2020

Published online:

- [1] A. D. de Oliveira, C. A. G. Beatrice, in *Nanocomposites – Recent Evolutions*, (Ed.: S. Sivasankaran) IntechOpen, London **2019**.
- [2] D. G. Papageorgiouian, I. A. Kinloch, R. J. Young, *Prog. Mater. Sci.* **2017**, 90, 75.
- [3] M. Bhattacharya, *Materials* **2016**, 9, 262.
- [4] T. Zhang, R. D. Rodriguez, I. Amin, J. Gasiorowski, M. Rahaman, W. Sheng, J. Kalbacova, E. Sheremet, D. R. T. Zahn, R. Jordan, *J. Mater. Chem. C* **2018**, 6, 4919.
- [5] W. Sheng, W. Li, D. Tan, P. Zhang, E. Zhang, E. Sheremet, B. V. K. J. Schmidt, X. Feng, R. D. Rodriguez, R. Jordan, I. Amin, *ACS Appl. Mater. Interfaces* **2020**, 12, 9797.
- [6] W. Sheng, I. Amin, C. Neumann, R. Dong, T. Zhang, E. Wegener, W.-L. Chen, P. Förster, H. Q. Tran, M. Löffler, A. Winter, R. D. Rodriguez, E. Zschech, C. K. Ober, X. Feng, A. Turchanin, R. Jordan, *Small* **2019**, 15, 1805228.
- [7] R. D. Rodriguez, A. Khalelov, P. S. Postnikov, A. Lipovka, E. Dorozhko, I. Amin, G. V. Murastov, J.-J. Chen, W. Sheng, M. E. Trusova, M. M. Chehimi, E. Sheremet, *Mater. Horiz.* **2020**, 7, 1030.
- [8] Y. Zhao, Q. Han, Z. Cheng, L. Jiang, L. Qu, *Nano Today* **2017**, 12, 14.
- [9] S. Chung, K. Cho, T. Lee, *Adv. Sci.* **2019**, 6, 1801445.
- [10] J. Lin, Z. Zhu, C. F. Cheung, F. Yan, G. Li, *J. Mater. Chem. C* **2020**, 8, 10587.
- [11] Y.-K. Liu, M.-T. Lee, *ACS Appl. Mater. Interfaces* **2014**, 6, 14576.
- [12] K. K. Kim, I. Ha, P. Won, D.-G. Seo, K.-J. Cho, S. H. Ko, *Nat. Commun.* **2019**, 10, 2582.
- [13] K. Trzciński, R. D. Rodriguez, C. Schmidt, M. Rahaman, M. Sawczak, A. Lisowska-Oleksiak, J. Gasiorowski, D. R. T. Zahn, *Adv. Mater. Interfaces* **2016**, 3, 1500509.
- [14] S. Delacroix, H. Wang, T. Heil, V. Strauss, *Adv. Electron. Mater.* **2020**, 6, 2000463.
- [15] H. Zhang, J. Zhang, G. Su, T. Zhou, A. Zhang, *Compos. Sci. Technol.* **2020**, 190, 108045.
- [16] P.-Y. Chang, C.-F. Lin, S. El Khoury Rouphael, T.-H. Huang, C.-M. Wu, D. Berling, P.-H. Yeh, C.-J. Lu, H.-F. Meng, H.-W. Zan, O. Soppera, *ACS Appl. Mater. Interfaces* **2020**, 12, 24984.
- [17] Y. Xie, L. Wen, J. Zhang, T. Zhou, *Mater. Des.* **2018**, 141, 159.
- [18] C. Liu, Y. Lu, Y. Xiong, Q. Zhang, A. Shi, D. Wu, H. Liang, Y. Chen, G. Liu, Z. Cao, *Polym. Degrad. Stab.* **2018**, 147, 115.
- [19] H. Zheng, G. C. Lim, *Opt. Lasers Eng.* **2004**, 41, 791.
- [20] C. Zhang, Y. Dai, G. Lu, Z. Cao, J. Cheng, K. Wang, X. Wen, W. Ma, D. Wu, C. Liu, *ACS Omega* **2019**, 4, 20787.
- [21] J. Feng, J. Zhang, Z. Zheng, T. Zhou, *ACS Appl. Mater. Interfaces* **2019**, 11, 41688.
- [22] P. Chang, A. Bruntz, L. Vidal, P. Vetter, P. Roudot, L. Bua, J. Ortiz, H. Zan, O. Soppera, *Macromol. Mater. Eng.* **2019**, 304, 1900402.
- [23] M. W. Knight, N. S. King, L. Liu, H. O. Everitt, P. Nordlander, N. J. Halas, *ACS Nano* **2014**, 8, 834.
- [24] H. U. Sverdrup, K. V. Ragnarsdottir, D. Koca, *Resour. Conserv. Recycl.* **2015**, 103, 139.
- [25] A. C. Ferrari, D. M. Basko, *Nat. Nanotechnol.* **2013**, 8, 235.
- [26] R. D. Rodriguez, Z. Khan, B. Ma, A. Mukherjee, P. Meszmer, J. Kalbacova, E. Garratt, H. Shah, J. Heilmann, A. R. Hight Walker, B. Wunderle, E. Sheremet, M. Hietschold, D. R. T. Zahn, *Phys. Status Solidi* **2019**, 216, 1900055.
- [27] J. Lin, Z. Peng, Y. Liu, F. Ruiz-Zepeda, R. Ye, E. L. G. Samuel, M. J. Yacaman, B. I. Yakobson, J. M. Tour, *Nat. Commun.* **2014**, 5, 5714.
- [28] L. Huang, J. Su, Y. Song, R. Ye, *Nano-Micro Lett.* **2020**, 12, 157.
- [29] Y. Dong, S. C. Rismiller, J. Lin, *Carbon* **2016**, 104, 47.
- [30] J. Wang, Z. Li, G. Fan, H. Pan, Z. Chen, D. Zhang, *Scr. Mater.* **2012**, 66, 594.
- [31] T. Etter, P. Schulz, M. Weber, J. Metz, M. Wimmeler, J. F. Löffler, P. J. Uggowitzer, *Mater. Sci. Eng., A* **2007**, 448, 1.
- [32] M. K. Trivedi, R. M. Tallapragada, A. Branton, D. Trivedi, G. Nayak, O. Latiyal, S. Jana, *J. Aeronaut. Aerosp. Eng.* **2015**, 4, 100142.
- [33] K. Geng, S. Li, Y. F. Yang, R. D. K. Misra, *Carbon* **2020**, 162, 465.
- [34] P. Hidalgo-Manrique, S. Yan, F. Lin, Q. Hong, I. A. Kinloch, X. Chen, R. J. Young, X. Zhang, S. Dai, *J. Mater. Sci.* **2017**, 52, 13466.
- [35] J. Kioseoglou, H. Le-Tran, S. Giaremis, I. Gelard, T. Ouisse, D. Chausse, E. Sarigiannidou, *Phys. Status Solidi* **2019**, 256, 1900037.
- [36] X. Liu, J. Li, E. Liu, Q. Li, C. He, C. Shi, N. Zhao, *Mater. Sci. Eng., A* **2018**, 718, 182.
- [37] W. Zhou, M. Dong, Z. Zhou, X. Sun, K. Kikuchi, N. Nomura, A. Kawasaki, *Carbon* **2019**, 141, 67.
- [38] B. Guo, B. Chen, X. Zhang, X. Cen, X. Wang, M. Song, S. Ni, J. Yi, T. Shen, Y. Du, *Carbon* **2018**, 135, 224.
- [39] C. Ma, D. Gu, D. Dai, H. Zhang, H. Zhang, J. Yang, M. Guo, Y. Du, J. Gao, *Surf. Coat. Technol.* **2019**, 375, 534.
- [40] A. E. Gheribi, M. F. Fini, L. Rivoalant, D. Lombard, G. Soucy, P. Chartrand, *Metall. Mater. Trans. B* **2020**, 51, 161.
- [41] X. Nie, H. Wang, J. Zou, *Appl. Surf. Sci.* **2012**, 261, 554.
- [42] N. T. Garland, E. S. McLamore, N. D. Cavallaro, D. Mendivelso-Perez, E. A. Smith, D. Jing, J. C. Claussen, *ACS Appl. Mater. Interfaces* **2018**, 10, 39124.
- [43] Y. Farazila, Y. Miyashita, W. Hua, Y. Mutoh, Y. Otsuka, *J. Laser Micro/Nanoeng.* **2011**, 6, 69.
- [44] Y. Kawahito, K. Nishimoto, S. Katayama, *Phys. Procedia* **2011**, 12, 174.
- [45] H. Wang, Y. Kawahito, K. Nishimoto, *IEEE Trans. Ind. Electron.* **2019**, 66, 1255.
- [46] M. R. Bobinger, F. J. Romero, A. Salinas-Castillo, M. Becherer, P. Lugli, D. P. Morales, N. Rodríguez, A. Rivadeneyra, *Carbon* **2019**, 144, 116.
- [47] V. Prakash, R. D. Rodriguez, A. Al-Hamry, A. Lipovka, E. Dorozhko, O. Selyshchev, B. Ma, S. Sharma, S. K. Mehta, V. Dzhagan, A. Mukherjee, D. R. T. Zahn, O. Kanoun, E. Sheremet, *Analyst* **2019**, 144, 3297.
- [48] V. V. Shumyantseva, T. V. Bulko, A. V. Kuzikov, R. Khan, A. I. Archakov, *Biochem. (Moscow) Suppl. Ser. B: Biomed. Chem.* **2014**, 8, 237.
- [49] M. He, Y. Wang, S. Wang, S. Luo, *Carbon* **2020**, 168, 308.
- [50] J. Liu, Y. Zou, B. Jin, K. Zhang, J. H. Park, *ACS Energy Lett.* **2019**, 4, 3018.
- [51] B. O. Burek, S. Bormann, F. Hollmann, J. Z. Bloh, D. Holtmann, *Green Chem.* **2019**, 21, 3232.

- [52] L. Jiao, W. Xu, H. Yan, Y. Wu, C. Liu, D. Du, Y. Lin, C. Zhu, *Anal. Chem.* **2019**, 91, 11994.
- [53] Z. Gu, Y. Wang, K. Feng, A. Zhang, *Process Saf. Environ. Prot.* **2019**, 130, 39.
- [54] H. W. Kim, M. B. Ross, N. Kornienko, L. Zhang, J. Guo, P. Yang, B. D. McCloskey, *Nat. Catal.* **2018**, 1, 282.
- [55] M.-R. Zhang, X.-Q. Chen, G.-B. Pan, *Sens. Actuators, B* **2017**, 240, 142.
- [56] O. Hosu, M. Lettieri, N. Papara, A. Ravalli, R. Sandulescu, C. Cristea, G. Marrazza, *Talanta* **2019**, 204, 525.
- [57] S. Upadhyay, S. Vaish, M. Dhiman, *Mol. Cell. Biochem.* **2019**, 450, 135.
- [58] G. Vilema-Enríquez, A. Arroyo, M. Grijalva, R. I. Amador-Zafra, J. Camacho, *Oxid. Med. Cell. Longevity* **2016**, 2016, 1908164.
- [59] Y. Shiraishi, T. Takii, T. Hagi, S. Mori, Y. Kofuji, Y. Kitagawa, S. Tanaka, S. Ichikawa, T. Hirai, *Nat. Mater.* **2019**, 18, 985.
- [60] L. Gao, J. Wu, D. Gao, *ACS Nano* **2011**, 5, 6736.
- [61] D. Harpaz, E. Eltzov, T. S. E. Ng, R. S. Marks, A. I. Y. Tok, *Diagnostics* **2020**, 10, 28.
- [62] R. D. Rodriguez, E. Sheremet, M. Nesterov, S. Moras, M. Rahaman, T. Weiss, M. Hietschold, D. R. T. Zahn, *Sens. Actuators, B* **2018**, 262, 922.
- [63] H. Tada, *Nanoscale Adv.* **2019**, 1, 4238.
- [64] C. Du, Q. Zhang, Z. Lin, B. Yan, C. Xia, G. Yang, *Appl. Catal., B* **2019**, 248, 193.
- [65] L. Zhou, Y. Tan, J. Wang, W. Xu, Y. Yuan, W. Cai, S. Zhu, J. Zhu, *Nat. Photonics* **2016**, 10, 393.
- [66] H. Yuk, B. Lu, S. Lin, K. Qu, J. Xu, J. Luo, X. Zhao, *Nat. Commun.* **2020**, 11, 1604.
- [67] D. S. Bergsman, B. A. Getachew, C. B. Cooper, J. C. Grossman, *Nat. Commun.* **2020**, 11, 3636.
- [68] X. Zhang, Y. Xu, M. Wang, E. Liu, N. Zhao, C. Shi, D. Lin, F. Zhu, C. He, *Nat. Commun.* **2020**, 11, 2775.
- [69] Y. Lu, H. Lyu, A. G. Richardson, T. H. Lucas, D. Kuzum, *Sci. Rep.* **2016**, 6, 33526.
- [70] C. Li, W. Zhao, *Natl. Sci. Rev.* **2020**, 7, 480.
- [71] R. D. Rodriguez, E. Sheremet, T. Deckert-Gaudig, C. Chaneac, M. Hietschold, V. Deckert, D. R. T. Zahn, *Nanoscale* **2015**, 7, 9545.